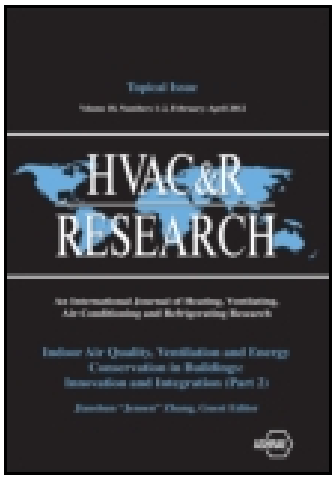

HVAC&R Research
Publication details, including instructions for authors and subscription information:
http://www.tandfonline.com/loi/uhvc20

An experimental and computational study of approach air distribution for slanted and A-shaped finned-tube heat exchangers

David A. Yashar[a], Piotr A. Domanski[b] & Honghyun Cho[c]

[a] Energy and Environment Division, National Institute of Standards and Technology, 100 Bureau Drive, Mailstop 7320, Gaithersburg, MD 20899-7320, USA

[b] HVAC&R Equipment Performance Group, National Institute of Standards and Technology, Gaithersburg, MD, USA

[c] Department of Mechanical Engineering, Chosun University, Gwangju, Korea

Published online: 01 Jul 2014.

To cite this article: David A. Yashar, Piotr A. Domanski & Honghyun Cho (2014) An experimental and computational study of approach air distribution for slanted and A-shaped finned-tube heat exchangers, HVAC&R Research, 20:5, 498-507, DOI: 10.1080/10789669.2014.899466

To link to this article: http://dx.doi.org/10.1080/10789669.2014.899466

HVAC&R Research (2014) **20**, 498–507
ISSN: 1078-9669 print / 1938-5587 online
DOI: 10.1080/10789669.2014.899466

Taylor & Francis
Taylor & Francis Group

An experimental and computational study of approach air distribution for slanted and A-shaped finned-tube heat exchangers

DAVID A. YASHAR[1,*], PIOTR A. DOMANSKI[2], and HONGHYUN CHO[3]

[1]*Energy and Environment Division, National Institute of Standards and Technology, 100 Bureau Drive, Mailstop 7320, Gaithersburg, MD 20899-7320, USA*
[2]*HVAC&R Equipment Performance Group, National Institute of Standards and Technology, Gaithersburg, MD, USA*
[3]*Department of Mechanical Engineering, Chosun University, Gwangju, Korea*

One of the most influential factors of the performance of a finned-tube heat exchanger is the distribution of the air passing through it; therefore, it must be known in order to produce a highly efficient design. We examined two different common style air-to-refrigerant, finned-tube heat exchangers: a single-slab coil oriented at an angle of 65° to the duct wall and an A-shaped coil with an apex angle of 34°. We used particle image velocimetry (PIV) to measure their in-situ airflow distributions. The results show that the airflow distributions for both heat exchangers are highly nonuniform with different sections being subject to vastly different air velocities. We also used a momentum resistance-based computational fluid dynamics (CFD) approach to model the airflow distributions through these heat exchangers. The modeled results agreed with the measured values, with most of the simulated velocities falling within +/-10% of the measured velocities. The results of this study show that the velocity profile for any configuration is strongly influenced by the geometry of the heat exchanger and other features in its proximity and, therefore, each installation configuration will have its own unique velocity distribution. The information presented in this paper documents the maldistribution of airflowing through finned-tube heat exchangers and highlights the sources and magnitude of the nonuniformities.

Introduction

The performance of an air-to-refrigerant, finned-tube heat exchanger is greatly influenced by the distribution of the air passing through it. The most basic function of the heat exchanger is to route the hot and cold fluids in such a way that they can thermally interact with each other in the most effective manner. If one of those fluids is not distributed properly in relation to the other fluid, then the heat exchanger will not perform this function well. To this end, there has been long standing interest in learning about air-side maldistribution. Fagan (1980) examined its effects on the performance of small heat exchangers used in room air conditioners. His study showed that typical air maldistributions commonly result in quite large velocity variations, and that the impact on performance is significant. Kirby et al. (1998) experimentally investigated the performance of a window air conditioner under wet and dry coil conditions. Their study showed that the coil face velocity on the evaporator varied by a factor of 3. Chwalowski et al. (1989) later showed similar results indicating large air velocity maldistributions and went on to demonstrate as much as a 30% variation in capacity for a given evaporator when subject to different airflow distributions.

Aganda et al. (2000) performed a numerical study of the effects of maldistributed airflow through the evaporator of a packaged air-conditioning unit equipped with a thermostatic expansion valve (TXV). Their study demonstrated that altering the airflow distribution could significantly change the overall performance of the system. They also concluded that the basis for the relationship between the airflow distribution and the system performance lies in individual circuits of the multi-circuit evaporator. This conclusion was reached because maldistributed air will cause each circuit to have a different amount of air available for heat exchange; each circuit will perform differently resulting in different exit conditions (degrees of superheat or two-phase quality). If liquid droplets are present in one or more refrigerant circuit exits, the TXV will reduce the total refrigerant mass flow rate through the evaporator in an effort to maintain the target level of superheat. The resulting reduced flow rate will cause a decrease in the total capacity.

Gong et al. (2008) studied the performance of a 50 kW water-to-air heat pump operating with several air distribution

Received October 18, 2013; accepted February 21, 2014
David A. Yashar, PhD, Member ASHRAE, is a Deputy Chief. **Piotr A. Domanski, PhD,** Fellow ASHRAE, is a Leader. **HongHyun Cho, PhD,** is an Assistant Professor.
*Corresponding author e-mail: dyashar@nist.gov
Color versions of one or more of the figures in the article can be found online at www.tandfonline.com/uhvc.

patterns. Their work showed that both the refrigerant evaporating temperature and refrigerant mass flow rate decreased as the level of air maldistribution increased. The overall result was a sharp decline in the system capacity and in the coefficient of performance (COP). This prior work also showed that the rate of frost accumulation on the evaporator is positively correlated to the level of air maldistribution. The studied system had to defrost more frequently at high levels of maldistribution, which additionally degraded the heat pump's overall performance.

Kaern et al. (2011) performed a simulation study on the effects of air maldistribution. They modeled an 8.8 kW residential air conditioner with a two-circuit evaporator and an electronic expansion valve (EEV) that maintained an overall superheat of 5 K. In the study, they fixed the total amount of air supplied to the evaporator and examined the impact of preferentially supplying a larger portion to one of the two identical circuits. The simulations showed that, for small levels of maldistribution, when one circuit received a larger portion of the total airflow than the other, the capacity of that circuit was larger than the baseline case where the airflow was evenly distributed between the circuits. The capacity of the other circuit, by comparison, was penalized to a higher level and the total capacity of the evaporator and the system COP both decreased. For larger levels of maldistribution, the circuit with less airflow would lose its ability to boil all of the refrigerant, thus resulting in two-phase refrigerant at the exit that, in turn, caused the EEV to reduce the total refrigerant mass flow rate through the evaporator. In the extreme case where 80% of the air was supplied to one circuit, the cooling capacity decreased 49.9 % and the system COP decreased 43.2 % from the baseline test case with uniform airflow. In a follow up study, Kaern et al. (2013) examined the effects of air maldistribution on two different common circuitry designs. This follow-up study showed, among other things, that the capacity and COP were influenced by the magnitude and pattern of the airflow maldistribution, and that a circuitry design which performs better than another with a given airflow distribution may perform worse than the other design if subject to a different airflow distribution.

While the focus of these referenced studies was to directly tie the system performance degradation with the magnitude of air maldistribution, they all demonstrate that how well the air and refrigerant distributions are matched throughout the heat exchanger is the key performance issue. The airflow distribution does not have to be uniform in order to achieve good heat exchanger performance; however, it does have to be well known so that the heat exchanger can be designed with the goal of routing the refrigerant through it in the best possible path. Recently, several researchers, including Abdelaziz et al. (2008), Singh et al. (2011), Wu et al. (2008), and Yashar et al. (2012), have demonstrated methods to design refrigerant circuitries that enable a heat exchanger to operate efficiently with a nonuniform air distribution.

Several researchers have examined ways to measure and model the airflow distribution approaching evaporators and condensers to help understand the sources and magnitude of air maldistribution. Lee et al. (2010) used a network of hotwire anemometers to measure the flowfields near multi-slab condensers and showed the variation of the air distribution with different included angles between the coils. Zhe et al. (2004) used a series of guide channels and gas turbine meters to measure airflow distribution through a plate fin heat exchanger. Their study showed very significant differences in local velocities through these heat exchangers, typically on the order of 2 to 1. The ultimate goal of this study is to demonstrate the impact of heat exchanger geometry, installation and associated features on the airflow distribution. Both laboratory measurements and computational fluid dynamics (CFD) modeling are used to pursue this goal.

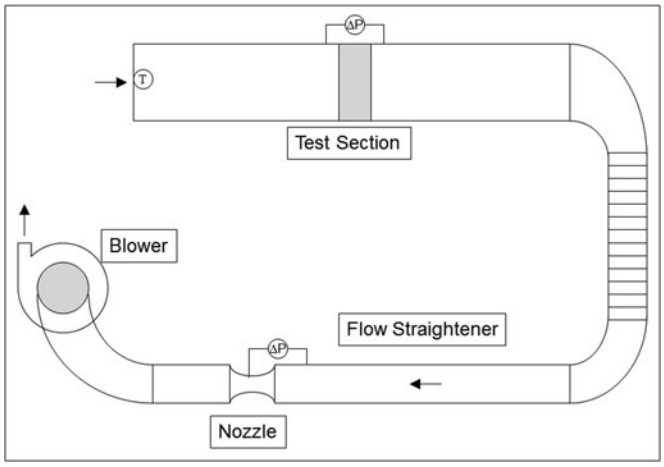

Fig. 1. Schematic of test setup.

Test setup and data acquisition

Figure 1 shows a schematic of the test setup. Airflows through the apparatus in the direction indicated by the arrows in the figure. Air enters from the laboratory environment and passes through the test section, which is comprised of a finned-tube

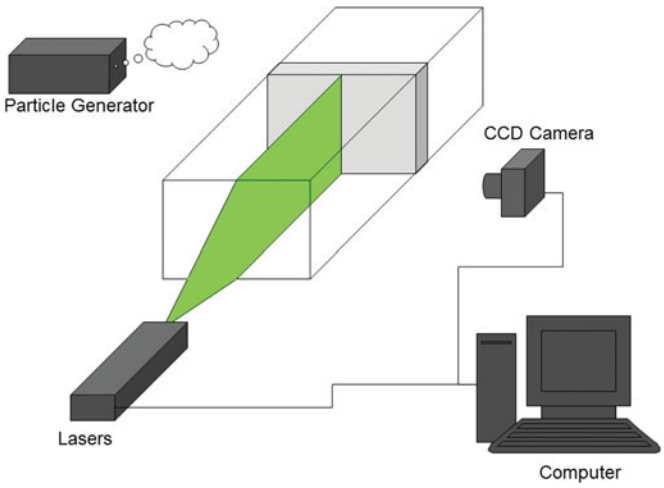

Fig. 2. PIV airflow measurement setup.

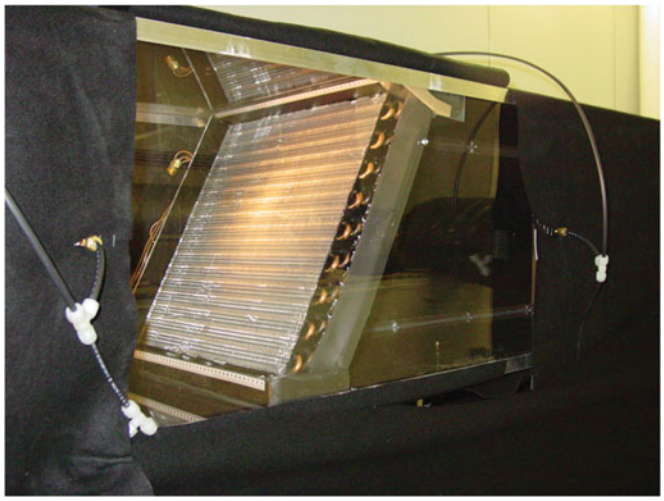

Fig. 3. Slanted coil test section.

heat exchanger secured in an acrylic section of duct. After the test section, the air passes through a flow straightener and then through a venturi nozzle that is used to measure the flow rate. A blower controlled by a variable-speed drive is positioned downstream of the venturi nozzle; it pulls the air through the test section and discharges it to the laboratory environment.

We measured the airflow distribution through the test section using particle image velocimetry (PIV), as this method provided the means to measure the airflow without creating disturbances. PIV uses laser generated light sheets to illuminate particles entrained in the flow field and synchronized photo snapshots to track their motion. Figure 2 shows the PIV setup with the position of the lasers relative to the test section, the laser-generated light sheets, and the camera. The method resulted in velocity measurements with a relative uncertainty typically less than 4% at 95% confidence. A thorough description of the airflow test setup, the PIV test setup and the associated measurement uncertainties can be found in Yashar et al. (2007).

Slanted coil air velocity distribution

Coil description

The slanted coil is a single-slab heat exchanger positioned at an angle of 65° to the duct wall. It is 455 mm tall, 430 mm wide, and 65 mm deep, and had 72 tubes among 4 rows and louvered fins. A plastic mounting bracket fastened to the lower portion of this heat exchanger is used to maintain the 65°-angle between the heat exchanger and the lower wall of the duct. A short metal sheet attached to the upper edge of the heat exchanger fastens the top of the heat exchanger to the upper wall of the duct. Figure 3 shows the position of the slanted coil within the test section. The measurements were taken when subjecting the heat exchanger to the manufacturer's rated airflow rate of 0.35 m^3/s standard air.

PIV measurement results for slanted slab

The lasers were aimed to capture the velocity distribution at the inlet to the test section along a vertical slice at the heat exchanger's midline. Figure 4 shows the component of the air velocity profile perpendicular to the coil surface. The data set displays a strong sinusoidal velocity pattern, which is caused by the tubes within the first depth row of the heat exchanger. There are 18 tubes per depth row in this heat exchanger; the position of each tube is identifiable by a local minimum in the velocity, as seen in Figure 4. The flow appears to have three distinctly separate regions, which illustrates the magnitude of the airflow nonuniformity. In the lower portion of the coil, corresponding approximately to the region between 0 and 50 mm from the bottom, the airflow rapidly increases as one moves away from the wall. The first tube near the bottom of the heat exchanger (and those occupying the same position within subsequent depth rows) receives very little airflow at all. In the region between 50 and 250 mm from the bottom of the coil, the flow rate is at its peak and is relatively constant. In the upper portion of the heat exchanger, from 250 to 455 mm, the air velocity gradually tapers because of the diminishing duct area. The tube nearest the top of the heat exchanger receives less than one third of airflow received by a tube positioned in the middle.

CFD simulation results for slanted slab

We generated a CFD model of the flow domain using the technique described by Yashar et al. (2011). In order to prepare a two-dimensional computational domain representative of the slanted coil's flow field, the domain was divided into three regions with a total of seven sub-domains; there were no available symmetry planes to simplify the domain. Figure 5 shows the representation of the flow domain, with each sub-domain labeled with roman numerals I through VII. The flow through the domain is from left to right.

The first region, composed of sub-domains I, II, and III, represents the duct inlet and the flow area upstream of the heat exchanger. The flow inlet is located at the left-most boundary, the upper and lower boundaries represent the duct walls, and the right-most boundary of sub-domain III represents the inlet surface of the heat exchanger. The second region is entirely comprised of sub-domain IV, which represents the heat exchanger positioned at a 65°-angle to the duct. This sub-domain was modeled using a momentum resistance modeling approach. The third region represents the computational domain downstream of the heat exchanger and is comprised of sub-domains V, VI, and VII. The airflow enters this region through sub-domain V on the left side, and exits through sub-domain VII on the right side. Note that sub-domain V is a very thin portion of the region. This sub-domain is needed to represent a short plate attached to the lower portion heat exchanger, which collects and directs water that condenses during operation. This plate is located at the backside of the heat exchanger, at a distance of 19 mm downstream, and follows the heat exchanger to a height of 51 mm above the lower duct wall.

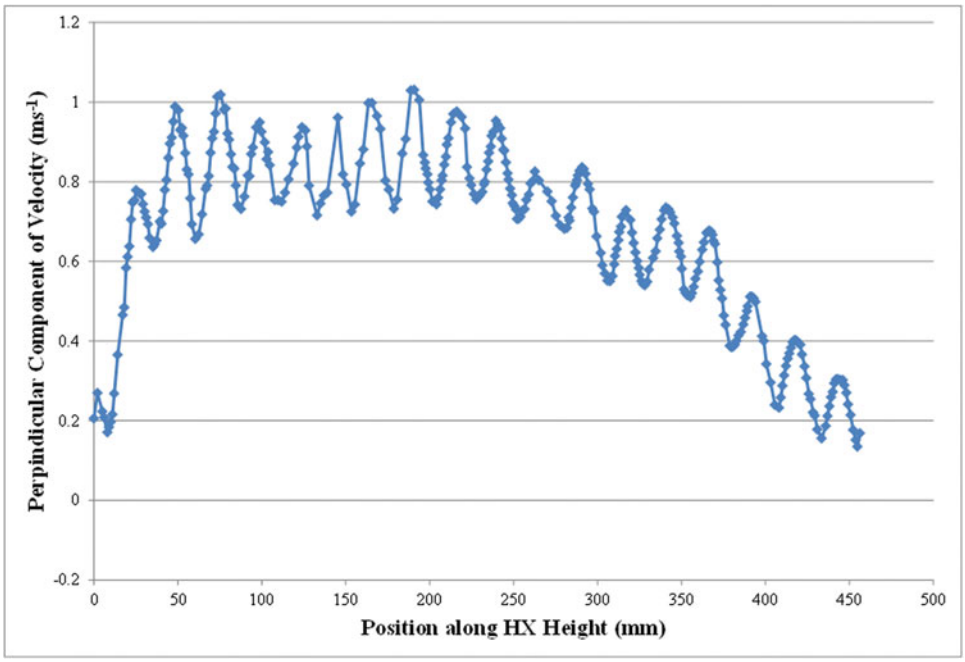

Fig. 4. Velocity profile for slanted coil test section.

We used constant velocity and pressure boundary conditions along the domain inlet, and constant farfield velocity and pressure boundary conditions were set along the domain outlet. The top and bottom of the flow domain represented the duct walls and therefore were set with no-slip boundary conditions. The short plate downstream of the heat exchanger, near the bottom of the duct, was modeled as a thin wall obstruction; therefore, no-slip boundary conditions were also set here. The Reynolds number for the air flowing through the duct was calculated from the total airflow rate and duct dimensions. $Re = 45{,}300$ was used to generate initial guesses for the boundary conditions of turbulence intensity, turbulent kinetic energy, and dissipation rate for input to the CFD solver's $k-\varepsilon$ turbulence model.

During the laboratory measurements, we collected 10 data points to correlate the air pressure drop through the coil to the airflow rates. This data was regressed to determine the quadratic and linear momentum resistance coefficients, K_q and K_l, by a least squares fit of the function:

$$\frac{\Delta P}{\Delta x} = \frac{\rho}{2}\left(K_q \bar{u}^2 + K_l \bar{u}\right)$$

where $\frac{\Delta P}{\Delta x}$ represents the pressure difference through the heat exchanger divided by its thickness, ρ represents the density of the air, and $\bar{u}$represents the average face velocity. The resulting quadratic and linear coefficients for this model were 227.71 m^{-1} and 358.67 s^{-1}, respectively. The momentum resistance model uses these coefficients to simulate the pressure drop imparted by flow through the narrow passages of the heat exchanger for all of the nodes within sub-domain IV. It is important to note that these coefficients are specific to this heat exchanger model and a coil with different fin design and/or spacing would have significantly different resistance coefficients.

In total, the computational domain consisted of 4375 nodes and the solver computed the results in approximately 10 hours with a 3.0 GHz processor. Figure 6 shows the velocity vector fields upon approach to the heat exchanger at five different locations measured from the duct inlet. The first two pictures in this sequence show image planes that are entirely upstream of the heat exchanger, the third picture (location 1118 mm) shows the point where the bottom of the image plane first touches the inlet surface of the heat exchanger, and the last two pictures show the plane passing through a portion of the

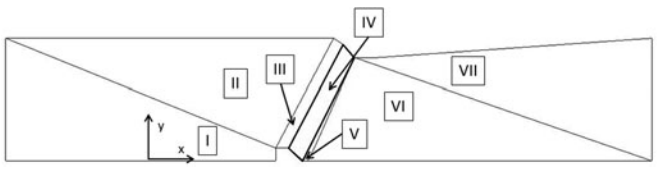

Fig. 5. Computational domain for slanted coil.

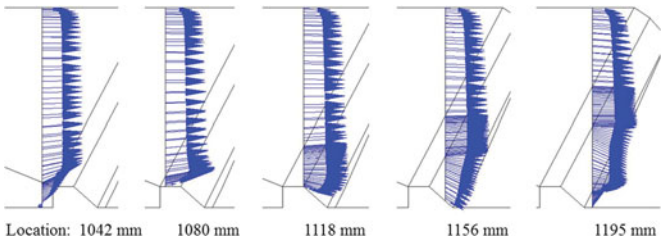

Fig. 6. Velocity vector profiles for slanted coil.

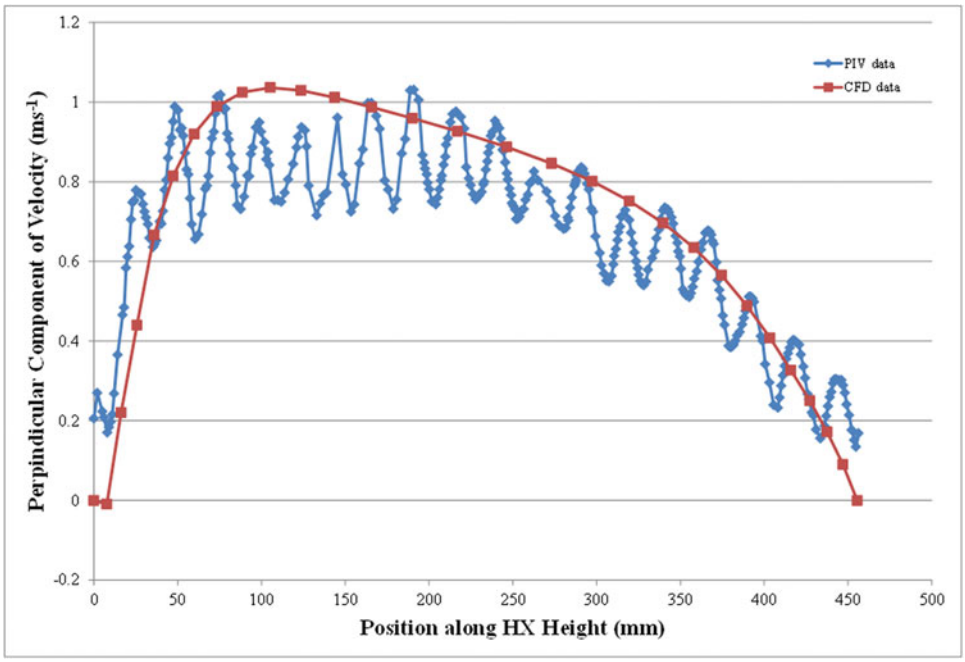

Fig. 7. Comparison of PIV and CFD data for slanted coil.

heat exchanger. In this sequence, we can see that the flow reacts to the mounting bracket by accelerating around it, causing an increase in the local flow rate near the lower portion of the heat exchanger.

Figure 7 shows the comparison of the CFD simulation results with the measured PIV data. Here, the velocity component perpendicular to the coil inlet surface is plotted against the position along the coil height. The predicted data and the measured data agree well with the obvious exception of the sinusoidal velocity component missing from the CFD results since the tube locations were not included in the model. The momentum resistance based CFD simulation predicts the velocity over most of the coil. Specifically, the model matches the measured data within 10% in the range of 150 mm through the top of the coil and also in the range of 25 through 100 mm. The model predicts slightly higher velocities in the range of 100 to 150 mm, but the predictions are within 15% of the measured velocity. In the lowest portion of the coil, 0–25 mm, the model predicts lower velocities, but the results are within 0.1 ms^{-1} of the measured values.

A-shaped coil air velocity distribution

Coil description

Figure 8 shows a photograph of the A-shaped coil mounted in the test section. The coil consists of two slabs assembled in such a way that it resembled the letter 'A' with an angle of 34° between the slabs. Each slab has 60 tubes (3 depth rows of 20 tubes) giving a total of 120 tubes in the dual-slab assembly. Each slab is 520 mm tall, 400 mm wide, and 65 mm deep. The tube fins are of the louver type.

This heat exchanger is designed for both vertical and horizontal installation. The sheet metal visible at the lower entry edge of the assembly is a condensate pan that was permanently attached to the bottom of the heat exchanger, although only truly needed for a vertical installation.

PIV measurement results for A-shaped coil

All tests were conducted at the manufacturer's rated airflow rate of 0.65 m^3/s standard air. PIV measurements were taken along the lateral midline of the heat exchanger. The

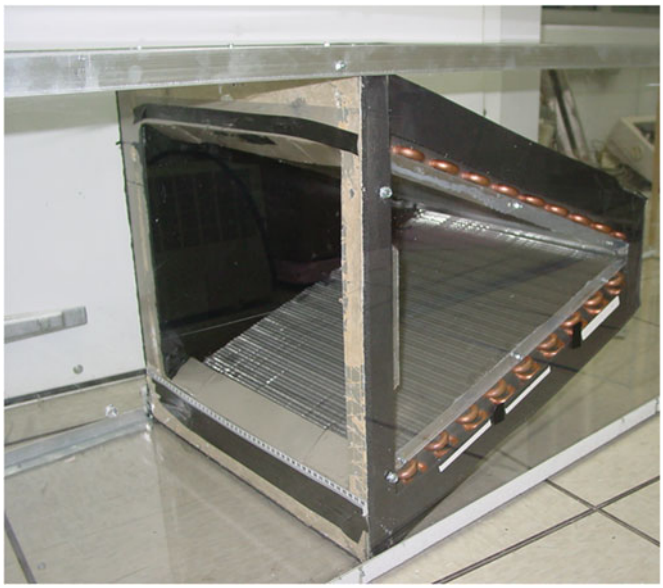

Fig. 8. A-shaped coil test section.

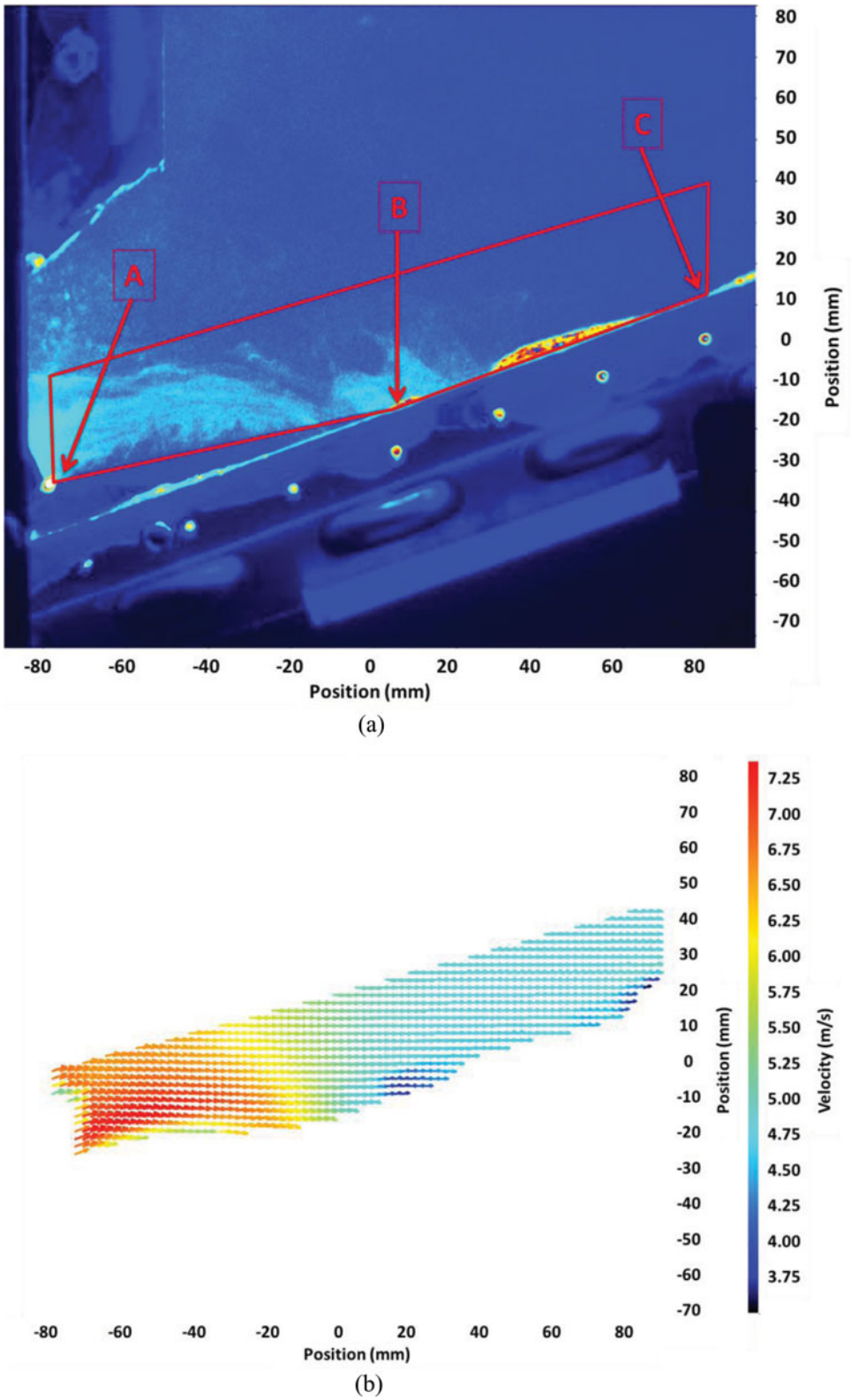

Fig. 9. a. Lower inlet portion of A-shaped coil. b. Resulting recirculation zone.

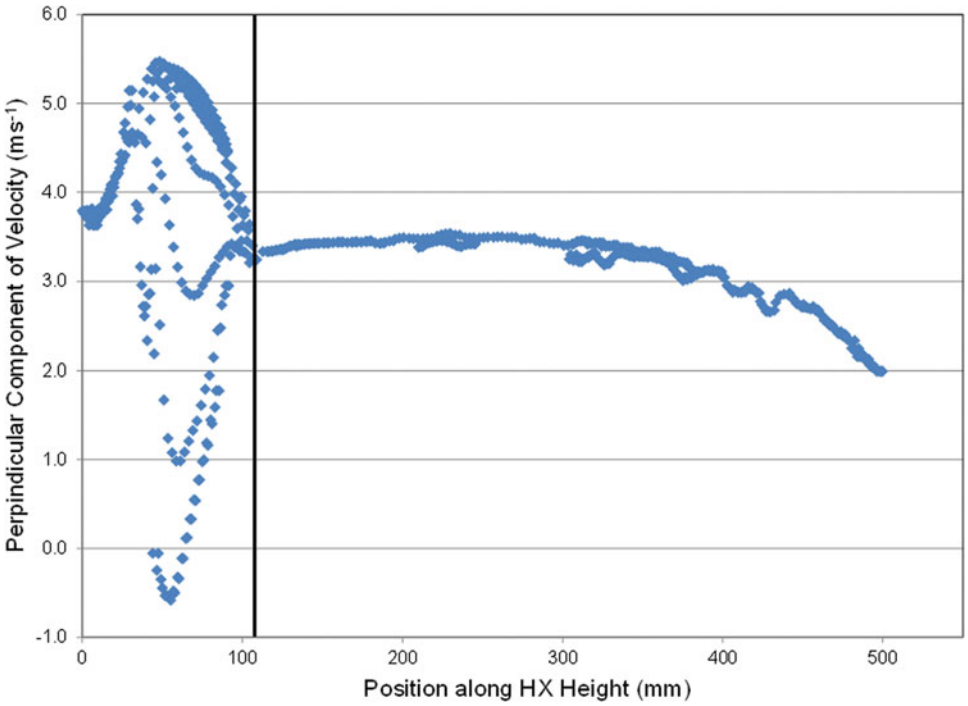

Fig. 10. Velocity profile for one slab of an A-shaped coil.

measurements revealed an interesting air recirculation zone near the inlet section of the heat exchanger. Figure 9a is a picture of the inlet portion of the lower slab with air flowing from left to right. A red polygon is overlaid onto this picture with points marked A, B, and C. The edge of condensate collection tray can be seen on the far left side of the figure at the leading edge of the airflow path, point A. The segment marked by points A and B show the lower bound on the area where data could be collected due to the shadow cast on the heat exchanger surface by the condensate tray; the shadow did not affect the data along the line between B and C.

The condensation collection tray acts as an airfoil and causes a recirculation zone between it and the coil, which effectively blocks the airflow to a significant portion of the coil. Figure 9b is the air velocity vector field calculated inside the red polygon outlined in Figure 9a.

Figure 10 shows the profile of the velocity component perpendicular to the inlet plane of the heat exchanger. The view of the bottom-most 105-mm portion of the heat exchanger surface was obstructed by the condensate pan and this segment could not be illuminated by the laser; therefore, PIV data could not be collected at that segment of the coil surface. For this reason, the data in Figure 10 is partitioned into two sections separated by a solid vertical line positioned at 105 mm from the bottom of the coil. The points to the left of the line represent the velocity data collected along a straight line between the edge of the condensate pan to the 105-mm position (shown as line AB on Figure 9a). The data to the right of the line represents the air velocity measured along the inlet surface from that point to the apex of the A-coil (line BC and extended past point C on Figure 9b).

The points to the left of the line were collected along a straight line that is not parallel to the heat exchanger surface; therefore the data collected along this segment is not directly scaled to the air mass flow into the coil, but it provides good insight to the recirculation generated by the pan and was included in this figure for completeness. The data to the left of the solid line is organized into several strands. Each strand represents data that was collected along a straight line parallel to the lowest edge of the illumination plane (e.g. the first strand was measured at the lowest edge and the second measured directly above it). The large velocity gradients provide a one-dimensional representation of the air swirling between the condensate pan and the coil. This data shows that the steepest velocity gradients occur in the vicinity of the third tube from the bottom of the coil, with flow away from the coil at the nearest measured point. This figure indicates that the bottom most 3 or 4 tubes in both slabs of the heat exchanger do not receive a significant amount of airflow and, therefore, cannot provide much heat transfer.

The observed large inefficient portion of the heat exchanger further emphasizes the importance of knowing the airflow

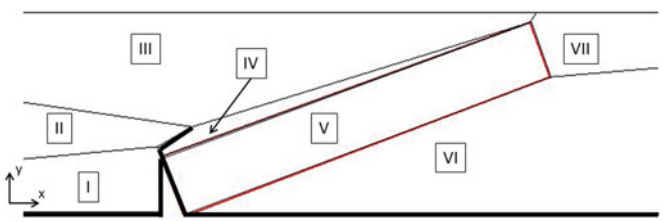

Fig. 11. Computational domain for A-shaped coil.

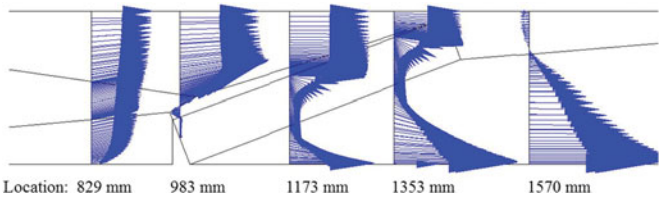

Fig. 12. Velocity vector profile for A-shape coil.

distribution for designing heat exchangers. In this case, approximately 20% of the entire heat exchanger provides little or no functionality. If the designers were aware of this airflow pattern, they could have developed a design that would accommodate this distribution while saving material costs.

CFD simulation results for A-shaped coil

The CFD simulations for the A-shaped coil involved a rather intricate geometry for the flow field. We began by preparing the geometrical domain for the solver in the same manner as for the slanted heat exchanger, two-dimensional and in alignment with the PIV measurement slice. The A-shaped coil did provide an opportunity for a simplification in the domain due to symmetry; therefore, only one slab of the heat exchanger was modeled in this domain.

Figure 11 shows a segment of the computational domain used for A-shape coil simulations. We divided the computational domain into three regions with a total of seven subdomains as shown. Sub-domains I through IV are upstream of the heat exchanger slab, sub-domain V represents the heat exchanger itself, and sub-domains VI and VII represent the flow domain downstream of the heat exchanger. The line segments that span the top portion of this figure represent the symmetry line that divides the two slabs of the heat exchanger. The lines along the lower portion of the figure represent the duct walls and the rigid obstructions connected to the heat exchanger slab. The rigid boundaries in this figure, specifically the duct wall and the condensate pan, are represented by the thick lines. The layout indicates that the flow coming from sub-domains I and II must accelerate around the edge of the condensate pan and approach the heat exchanger through sub-domain III. All flow into the heat exchanger must, therefore, pass through sub-domain III then through sub-domain IV before entering sub-domain V.

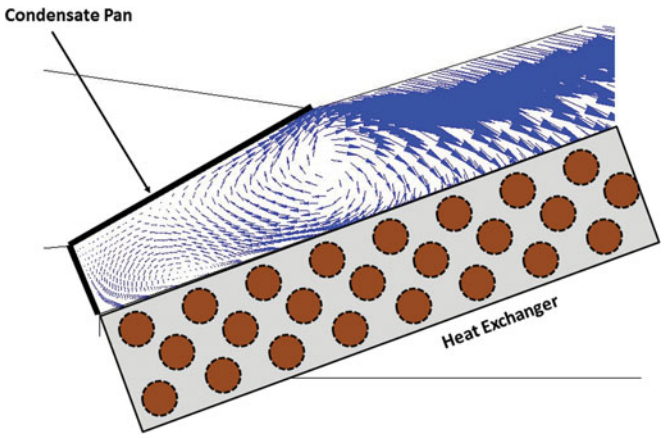

Fig. 13. Recirculation zone for A-shaped coil simulated by the CFD model.

We next determined the parameters for use in the CFD solver's k-ε turbulence model. We used measured laboratory data to determine the Reynolds number for the flow (82,900), and then generated initial guesses for the boundary conditions of turbulence intensity, turbulent kinetic energy, and dissipation rate. We also determined the momentum resistance coefficients for sub-domain V based on curve fitting a series of 10 measured data points of pressure drop through the coil vs. airflow rate; the values were 435.99 m^{-1} and 95.42 s^{-1} for the quadratic and linear resistance coefficients, respectively.

In total, the computational domain consisted of 7350 nodes and the solver computed the results in approximately 18 h with a 3.0-GHz processor. Figure 12 presents the simulation results in the vector form in depicting a series of velocity distribution patterns along the length of the computational domain. The first velocity distribution pattern shown upstream of the heat exchanger is a typical pattern found in unobstructed turbulent flow. At the second position, the velocity distribution gets quite interesting. Along this line, most of the locations realize forward moving flow; however, the region between the condensate pan and the heat exchanger slab is flowing backwards. The third and fourth position show how the flow passes through the heat exchanger and then changes the course to flow down the duct towards the exit plane. The fifth position shows the flow adjusting itself to the full open duct with some backwards flow caused by recirculation downstream of the coil's apex.

Since we have computationally solved the entire flow domain, we can readily extract the velocity at any point within the domain, unlike with the PIV measurements where we are limited by the line of sight. Figure 13 shows the computed vector field for the lower portion of sub-domain IV. The CFD simulation predicted a very similar recirculation zone to that indicated by the PIV measurements.

Figure 14 shows the perpendicular component of the velocity field entering the lower slab of the heat exchanger, as computed by the CFD model. The simulation results concur with the measurements in that a large portion of this heat exchanger is starved for air along the very bottom-most portion of the coil, between 0 and 21 mm from the edge. Between 21 and 80 mm, the airflow is actually moving away from the coil. Above about 80 mm, a somewhat conventional airflow pattern is established.

Figure 14 also shows the PIV measured data for comparison with the simulation results. The data agree well for the middle portion of the heat exchangers with some deviations at the low region and, to a smaller degree, at the upper region of the heat exchanger near the coil's apex. The apparent significant differences between the computed velocity field and the measurements in the lower region can be explained by the very large velocity gradients in the region near the condensate pan, which make the results very sensitive to the location. For this reason, Figure 14 shows two strands of CFD data. The first set is the velocity computed at 0.2 mm upstream of the heat exchanger inlet, and the second set is the profile for

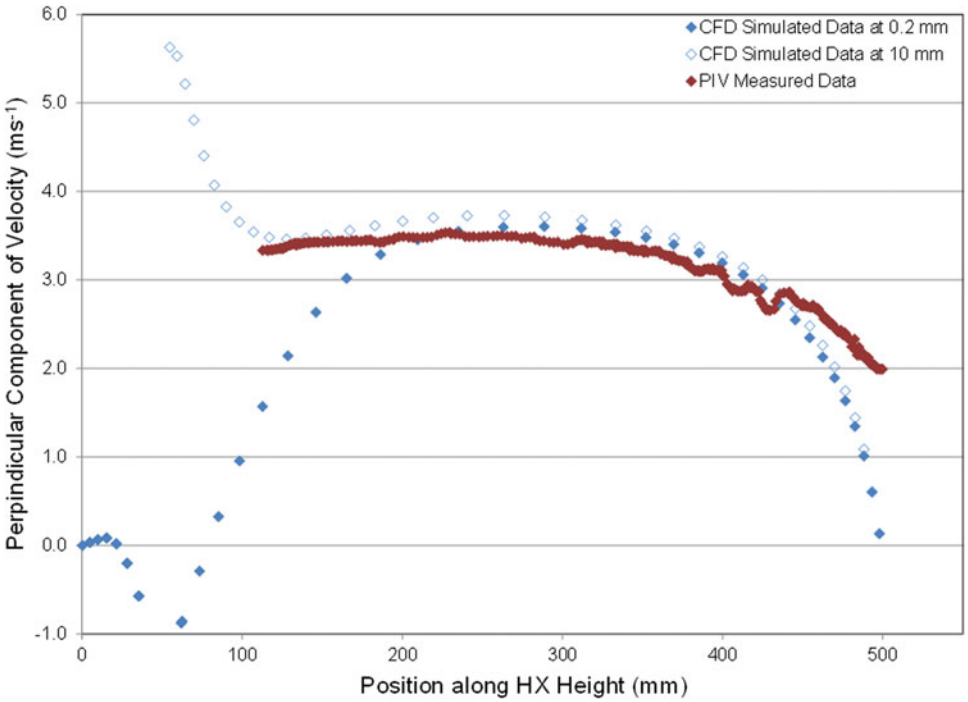

Fig. 14. Comparison of PIV data with CFD simulation results at 0.2 mm and 10 mm upstream of A-shaped coil.

the location10 mm upstream. While best efforts were taken to consistently collect PIV data at the same distance from the coil inlet, the data were collected 4 ± 2 mm upstream of the coil. The data at the coil surface was not useable due to the heat exchanger's mounting rail causing light reflections that corrupted the PIV data in that vicinity; the reflections were unavoidable. Regardless, the two sets of CFD data do bound the PIV measurements. Overall, the CFD and PIV results agree within 5% of the measured value over 90% of the coil surface.

Summary and conclusions

We examined the inlet air distribution for two common finned-tube heat exchangers. We measured the air velocity profile using PIV and performed CFD simulations for the tested setups and replicated the measured airflow velocity distribution patterns. We have observed a few consistencies for both tested heat exchangers. The most important point is that the airflow is generally nonuniform. The fins and tubes of the heat exchanger provide significant resistance to the airflow, which typically has the effect of evening out the distribution; however, it seems that other factors are more influential on the airflow distribution. The presence of any irregularities in the duct boundaries or heat exchanger mounting significantly alters the airflow and has a much more profound impact than the flow resistance due to the fins.

The slanted single slab heat exchanger showed a very nonuniform airflow distribution pattern because the heat exchanger was positioned at an angle and abrupt area changes were introduced by the mounting brackets. The measurements for this test subject showed that there was a high flow region caused by the acceleration of the airflow around the lower mounting bracket. Also, the measurements showed that positioning the coil at an angle caused about half of the coil to be subject to a somewhat linearly declining air velocity profile. The A-shaped coil had some similarities to that of the slanted coil. The A-shaped coil showed a relatively linearly declining air velocity profile as we moved closer towards the apex, although not as pronounced as seen on the slanted coil. More significantly, though, the condensate pan attached to this coil was an obstructive feature, which severely reduced the air supply to approximately one-fifth of the entire heat exchanger.

This study also shows that a simple momentum resistance based CFD model can be used to generate a reasonable prediction of the airflow velocity distribution through a finned tube heat exchanger. However, it must be noted that the two-dimensional approach described in this work was verified for flow situations where significant three-dimensional effects were not introduced to the test setup; therefore, the methods may not carry over directly to model systems with large three-dimensional flow fields.

References

Abdelaziz, O., V. Singh, V. Aute, and R. Radermacher. 2008, A-type heat exchanger simulation using 2-d cfd for airside heat transfer and pressure drop. *International Refrigeration and Air Conditioning Conference, Purdue University*, *West Lafayette, IN*, *July 14–17*.

Aganda, A.A., J.E.R. Coney, and C.G.W. Sheppard. 2000, Airflow maldistribution and the performance of a packaged air conditioning unit evaporator. *Applied Thermal Engineering* 20:515–28.

Chwalowski, M., D.A. Didion, and P.A. Domanski. 1989. Verification of evaporator computer models and analysis of performance of an evaporator coil. *ASHRAE Transactions* 95(1): 793–802.

Fagan, T.J. 1980. The effects of airflow maldistributions on air-to-refrigerant heat exchanger performance. *ASHRAE Transactions* 86(2):699–715.

Gong, J., G. Tieyu, Y. Xiuling, and H. Dong. 2008. Effects of airflow maldistribution on refrigeration system dynamics of an air source heat pump chiller under frosting conditions. *Energy Conversion and Management* 49:1645–51.

Kaern, M.R., W. Brix, B. Elmegaard, and L.F.S. Larsen. 2011. Performance of residential air-conditioning systems with flow maldistribution in fin-and-tube evaporators. *International Journal of Refrigeration* 34:696–706.

Kaern, M.R., B. Elmegaard, and L.F.S. Larsen. 2013.Comparison of fin-and-tube interlaced and face split evaporators with flow maldistribution and compensation, *International Journal of Refrigeration* 36:203–14.

Kirby, E.S., C.W. Bullard, and W.E. Dunn. 1998. Effect of airflow nonuniformity on evaporatory performance. *Transactions of the American Society of Heating, Refrigeration and Air Conditioning Engineers* 104(2):755–62.

Lee, T.S., W.C. Wu, Y.K. Chuah, and S.K. Wang. 2010. An improvement of airflow and heat transfer performance of multi-coil condensers by different coil configurations. *International Journal of Refrigeration* 33:1370–76.

Singh, V., O. Abdelaziz, V. Aute, and R. Radermacher. 2011. Simulation of air-to-refrigerant fin-and-tube heat exchanger with CFD-based air propagation. *International Journal of Refrigeration* 34:1883–97.

Wu, Z.G., G.L. Ding, K.J. Wang, and M. Fukaya. 2008. Knowledge-based evolution method for optimizing refrigerant circuitry of fin-and-tube heat exchangers. *HVAC&R Research* 14(3):435–52.

Yashar, D.A., and H.H. Cho. 2007. Air side velocity distribution in finned-tube heat exchangers. NISTIR 7474, National Institute of Standards and Technology, Gaithersburg, MD.

Yashar, D.A., P.A. Domanski, and H.H. Cho. 2011. An experimental and computational study of approach air distribution for a finned-tube heat exchanger. *HVAC&R Research* 17(1):76–85.

Yashar, D.A., J. Wojtusiak, K. Kaufman, and P.A. Domanski. 2012. A dual mode evolutionary algorithm for designing optimized refrigerant circuitries for finned-tube heat exchangers. *HVAC&R Research* 18(5):834–44.

Zhe, Z., L. Yanzhong., and X. Qing. 2004. Experimental research on flow maldistribution in pleat-fin heat exchangers. *Chinese Journal of Chemical Engineering* 12(1):7–13.